ACS APPLIED MATERIALS & INTERFACES

www.acsami.org

Research Article

Highly Reproducible Hyperthermia Response in Water, Agar, and Cellular Environment by Discretely PEGylated Magnetite Nanoparticles

Idoia Castellanos-Rubio,* Irati Rodrigo, Ane Olazagoitia-Garmendia, Oihane Arriortua, Izaskun Gil de Muro, José S. Garitaonandia, Jose Ramón Bilbao, M. Luisa Fdez-Gubieda, Fernando Plazaola, Iñaki Orue, Ainara Castellanos-Rubio, and Maite Insausti*

Cite This: *ACS Appl. Mater. Interfaces* 2020, 12, 27917−27929

Read Online

ACCESS | Metrics & More | Article Recommendations | Supporting Information

ABSTRACT: Local heat generation from magnetic nanoparticles (MNPs) exposed to alternating magnetic fields can revolutionize cancer treatment. However, the application of MNPs as anticancer agents is limited by serious drawbacks. Foremost among these are the fast uptake and biodegradation of MNPs by cells and the unpredictable magnetic behavior of the MNPs when they accumulate within or around cells and tissues. In fact, several studies have reported that the heating power of MNPs is severely reduced in the cellular environment, probably due to a combination of increased viscosity and strong NP agglomeration. Herein, we present an optimized protocol to coat magnetite (Fe_3O_4) NPs larger than 20 nm (FM-NPs) with high molecular weight PEG molecules that avoid collective coatings, prevent the formation of large clusters of NPs and keep constant their high heating performance in environments with very different ionic strengths and viscosities (distilled water, physiological solutions, agar and cell culture media). The great reproducibility and reliability of the heating capacity of this FM-NP@PEG system in such different environments has been confirmed by AC magnetometry and by more conventional calorimetric measurements. The explanation of this behavior has been shown to lie in preserving as much as possible the magnetic single domain-type behavior of nearly isolated NPs. *In vitro* endocytosis experiments in a colon cancer-derived cell line indicate that FM-NP@PEG formulations with PEGs of higher molecular weight (20 kDa) are more resistant to endocytosis than formulations with smaller PEGs (5 kDa), showing quite large uptake mean-life (τ > 5 h) in comparison with other NP systems. The *in vitro* magnetic hyperthermia was performed at 21 mT and 650 kHz during 1 h in a pre-endocytosis stage and complete cell death was achieved 48 h posthyperthermia. These optimal FM-NP@PEG formulations with high resistance to endocytosis and predictable magnetic response will aid the progress and accuracy of the emerging era of theranostics.

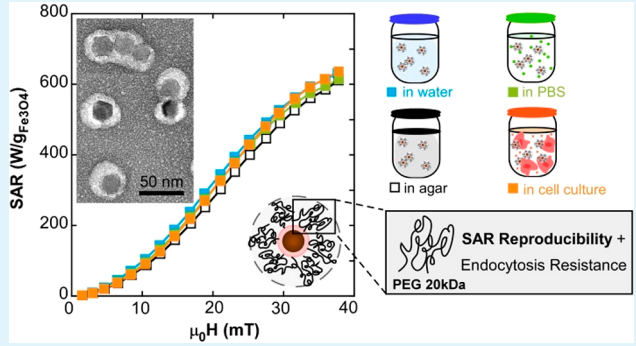

KEYWORDS: *magnetite-nanoparticles, AC magnetometry, PEGylation, dipolar-interactions, endocytosis, magnetic-hyperthermia, cell-death*

INTRODUCTION

Magnetic nanoparticles (MNPs) are becoming more in demand in the biomedical field due to their wide versatility.[1,2] Their dual function, as magnetic hyperthermia agents in cancer treatments and as contrast enhancement agents in magnetic resonance imaging (MRI), has made them grow into a paradigm in the theranostics field.[3] In magnetic hyperthermia therapies, the heat generated by MNPs under an alternating magnetic field (AMF) is used to increase the temperature in the tumor area. As healthy cells present higher resistance to heat, the tumor cells can be selectively driven to apoptosis (at 42−46 °C) without damaging healthy tissues.[4,5] The capacity of the MNPs to heat is measured through the specific absorption rate (SAR) which depends on both the AMF excitation conditions and the features of the MNPs (saturation magnetization, magnetic anisotropy, size, agglomeration degree, and so forth).[6] Magnetic hyperthermia treatment holds great promise as an effective cancer treatment with minimal side effects and it aims to become an alternative to chemo- and radiotherapies. One of the key points to reach a relevant improvement in this field is to attain nanoparticle

Received: February 20, 2020
Accepted: May 28, 2020
Published: May 28, 2020

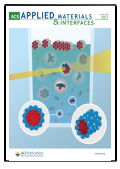

https://dx.doi.org/10.1021/acsami.0c03222
ACS Appl. Mater. Interfaces 2020, 12, 27917−27929

formulations whose therapeutic efficiency stays unchangeable regardless of the biological environment (different human tissues, organs, and so forth).

Nowadays MNPs of magnetite are considered one of the best choices for biomedical applications because of their high magnetic response and their good biocompatibility and biodegradability; in fact, several formulations of magnetite-based NPs have already gained approval for use in humans by the Food and Drug Administration (FDA).[7] However, the utility of magnetite MNPs in biomedicine has two serious limitations. First, their efficiency is severely restricted by the rapid elimination through innate host defense mechanisms as opsonization and phagocytosis.[8] Fortunately, stealthiness toward the immune system can be achieved by coating the nanoparticles with hydrophilic, nonionic, and biocompatible molecules as polyethilenglicol (PEG).[9] It has been demonstrated that PEGylation of NPs prolongs circulation time in the blood, improves colloidal stability, reduces cytotoxicity, and increases tumor accumulation.[10−12] PEGylation technology has also been proven to minimize the cell surface binding that drives to NP endocytosis,[13] delaying the intracellular biodegradation and increasing the therapeutic time window. Thus, MNPs appropriately coated by PEG molecules could overcome this first limitation. The second major handicap in the use of magnetite MNPs is the lack of reproducibility in their heating capacity. Apart from the difficulty to prepare replicable batches of MNPs, the hyperthermia response becomes rather weak and nonsystematic when the MNPs are placed in biological media.[14] The decrease of hyperthermia performance becomes more dramatic at long-term (>12 h), because of the intracellular biodegradation that occurs after cellular uptake of the MNPs.[15] In addition, as each biological system (*in vitro* and *in vivo*) presents its own physiological condition (viscosity, pH, ionic strength, and so forth), the aggregation state of the MNPs can vary widely depending on the environment. There are several studies analyzing how the SAR decreases when the MNPs are within cell environments, coming to very different conclusions. Some of these works conclude that hyperthermia performance decreases more when the MNPs are internalized compared to when they are on the cell membrane.[14,16] On the contrary, a recent study shows that the hyperthermia efficiency drops as soon as the MNPs are in the cellular media regardless of their extra- or intracellular location.[17] On the other hand, other studies defend that hyperthermia therapy can be even more successful after endocytosis of the MNPs.[18,19] This controversy could be due to the different nature of the studied MNPs (coating thickness, surface charge, shape, and so forth) that has great impact in their tendency to assemble into diverse 2D or 3D structures, causing very variable heating performances. Large and chaotic agglomerations of MNPs entail intense magnetic dipolar interactions and a very significant reduction of SAR values.[20] This interaction effect becomes sharply reinforced with the increase of MNP size. However, if the agglomeration process can be kept below certain limits, larger MNPs, which bring permanent or fixed magnetic moments (FM-NPs), produce higher SAR values than superparamagnetic NPs (SP-NPs), at least at high enough magnetic fields.[21] Recently, we developed a novel approach to load monolayers of FM-NPs with minimal agglomeration within targetable microdisks, achieving an optimized local heating on cell membranes for efficient cellular excitation.[22] Another recent work shows that two-dimensional magnetic nanobeads within solutions of different viscosities are able to maintain the SAR values almost unaltered.[23]

Herein, we present optimized FM-NP@PEG formulations with minimal dipolar interactions and considerable resistance to endocytosis. We have improved a surface modification strategy by coating magnetite FM-NPs individually or quasi-individually with long PEG molecules, a task of great complexity due to the tendency of FM-NPs to bunch up. This quasi-individual coating has been adjusted to different FM-NPs sizes and it is able to avoid further NP agglomeration in very diverse conditions, providing completely reproducible SAR values in distilled water, physiological solutions, agar, and cell culture media. SAR measurements of FM-NPs in such different media have been carried out accurately by measuring their dynamical hysteresis loops under H_{AC} conditions. Additionally, we have investigated the effect of PEG length on cytotoxicity and endocytosis resistance of the magnetite FM-NP systems in an *in vitro* model using the colon cancer-derived cell line HCT116. We have also performed a magnetic hyperthermia treatment *in vitro*, keeping the temperature of the cell culture within the therapeutic window and monitoring the temperature evolution in the cell cultures by calorimetry measurements. Our study demonstrates the great heating reproducibility of these FM-NPs@PEG formulations and its reliable efficiency to induce apoptosis in a pre-endocytosis stage. To the best of our knowledge this is the first time that a magnetite NP system with such high and systematic heating performance has been developed.

RESULTS AND DISCUSSION

Design of Optimal Fe_3O_4 FM-NP@PEG Formulation. Reproducible and systematic heat nanoinductors should be composed of pure, homogeneous, and good quality materials. It is widely known that the synthesis of monophasic magnetite NPs larger than 20 nm with low dispersity of size and shape is quite challenging.[24,25] The magnetic cores of our formulations were prepared based on a recently published method,[21] in which the shape and size of the FM-NPs is tuned by adjusting the amount of oleic acid, the final temperature of synthesis and the reflux time (see Materials and Methods). TEM micrographs in Figure 1a show monodisperse cuboctahedral nanoparticles of two different sizes: 23 nm (sample A) and 29 nm (sample B).

These average dimensions match very well with the crystallite sizes obtained from XRD (Table 1 and Table S1 in the Supporting Information), meaning that samples A and B are composed of single crystals. Both XRD and electron diffraction (ED) are compatible with magnetite phase (PDF #880866) and do not present any trace of wustite (see Figure 1d) which is a very common byproduct in this kind of iron oxide nanoparticles.[26,27]

The high purity of the iron oxide phase in the two samples was confirmed by the ^{57}Fe Mössbauer spectroscopy and magnetization measurements as a function of temperature and field, which are presented in Figure 2. The Mössbauer spectra of samples A and B were successfully fitted with two sextets whose parameters are collected in the tables of Figure 2a. As profusely discussed in the literature,[28] the two sextets corresponded to Fe^{3+} ions in tetrahedral sites (larger hyperfine field of ∼48 T, pale green-colored spectrum) and $Fe^{2.5+}$ intermediatevalence ions in octahedral sites (smaller hyperfine field of ∼45 T, dark green-colored spectrum). It is to note that relative areas of the two sextets ($x_{MS} = Fe^{2+}_{tet}/Fe^{2.5+}_{oct}$) was around

https://dx.doi.org/10.1021/acsami.0c03222
ACS Appl. Mater. Interfaces 2020, 12, 27917−27929

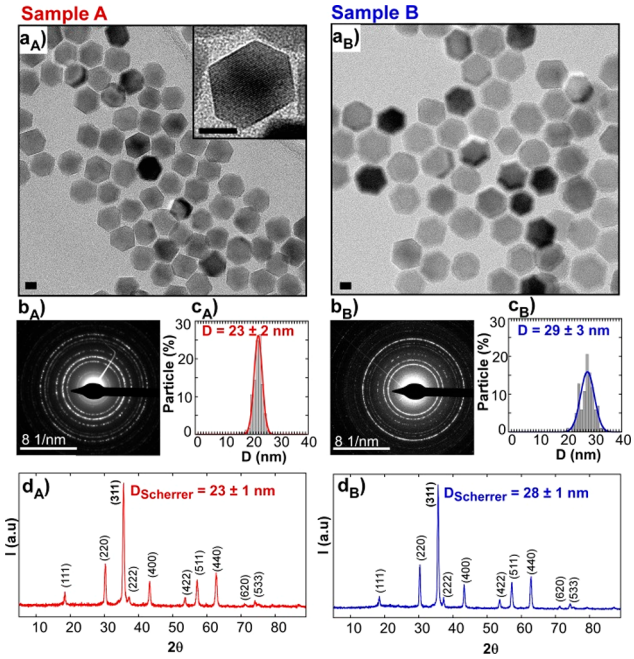

Figure 1. (a) TEM micrographs, (b) ED patterns, (c) size distributions, and (d) XRD patterns of Sample A and Sample B. Scale bars: 10 nm.

0.7 in both samples, a bit larger than expected (0.5) for perfectly stoichiometric magnetite. It means that the magnetite phase was slightly nonstoichiometric, probably due to existence of few Fe^{2+} vacancies in the octahedral sites, as has been suggested in similar studies.[29] In any case, particle magnetization almost reached that of pure magnetite (92 A·m^2/kg) in both samples (85 and 90 A·m^2/kg, as shown in Table 1), which is essential to achieve high heating rates. Additionally, magnetization versus temperature curves (ZFC/FC) displayed the characteristic hallmark of magnetite, Verwey transition, (Figure 2b) as a sudden step of the susceptibility at the vicinity of 100 K. The susceptibility step, better seen in the derivative of the ZFC curve, was located below 100 K (at 80 and 90 K). This shift suggested the moderately nonstoichiometric character of the samples, in agreement with the Mössbauer spectra and related systems in the literature.[30] At this point, it is also noteworthy to mention that wider lines in sample A were related to the higher thermal fluctuations of smaller NPs. This effect was also visible in the magnetic measurements as a function of temperature and field; the susceptibility step of ZFC was substantially wider in sample A (Figure 2b$_A$) and its hysteresis loop at room temperature showed almost zero hysteresis (Figure 2c$_A$). This indicated that certain particle population in sample A had an almost negligible permanent magnetic moment and so, it was close to the superparamagnetic regime.

On the other hand, it is worth noting the excellent fit of the hysteresis loops obtained at 5 K within the Stoner−Wohlfart model of uniaxial magnetic single domains. The monoclinic distortion of magnetite lattice at low temperature endowed crystalline magnetic anisotropy with a strong uniaxial character: the reduced remanent magnetization became close to 0.5, exactly as expected for randomly oriented isolated particles with uniaxial anisotropy. In fact, the simulations of the hysteresis loops in this framework rendered a very fine match with the experimental loops (Figure 2c$_{A,B}$) by simply implementing a normal distribution of uniaxial anisotropy constants (Model S2, Supporting Information). Such distribution can physically represent a "disorder" of shapes and/or lattice distortions. For instance, TEM images of Figure 1a showed slightly different elongations of particle facets, which involves the existence of a distribution of shape anisotropies. The best fits to the experimental loops at 5 K were obtained with a standard deviation of 5 kJ/m^3 and with average effective anisotropy constants of 24 kJ/m^3 (sample A) and 27.5 kJ/m^3 (sample B) (see Table 1), which are in accordance with the values reported in literature for magnetite.[31,32]

An essential step to convert the as-synthesized hydrophobic FM-NPs into stable aqueous colloid is to perform a surface modification of the nanoparticles. These nanoparticles were first coated with poly(maleic anhydride-*alt*-1-octadecene) (PMAO) and easily dispersed in distillate (D.I.) water, thanks to the large amount of carboxylate anions (Pz ≈ −40 mV; Table S2 Supporting Information). However, when the FM-NPs@PMAO are placed in physiological solutions the salt ions screen the surface charges provoking an instant aggregation. One way to achieve an enhancement of the colloidal stability in physiological media is to modify the surface of the NP with an amphiphilic copolymer that contains long PEG tails, such as PMAO-grafted PEG copolymer.[33,34] This kind of coating provides good stability in saline solutions as long as enough PEG molecules are grafted into the PMAO backbone. We prepared three copolymers of different molecular weights (M_W) by grafting PEG molecules (5, 10, and 20 kDa) into PMAO using 75% of its monomers. For simplicity, the coating protocol with PMAO−PEG was refined using the smallest FM-NPs (23 nm, sample A). First of all, sample A was coated with PMAO−PEG following a standard protocol;[35] this gave rise to collective coatings with the three copolymers (5, 10, and 20 kDa), as can be observed in Figure 3b. Although these clusters had an average dimension of around 500 nm (Table S2 Supporting Information), their thick polymeric coating allowed them to be stable in both distilled water and physiological media. Conversely, when sample A was coated only with PMAO and dispersed in distilled water, NPs did not form such large clusters; in fact, this negatively charged thin polymeric layer promotes a magnetic interaction that favors the formation of FM-NP chains (Figure 3a). But as PMAO coating does not confer colloidal stability to the FM-NPs in saline solutions, the

Table 1. Summary of the Mean Particle Dimension[a]

sample	$D_{TEM} \pm \sigma$ (nm)	$D_{XRD\text{-}311} \pm \sigma$ (nm)	M_s at RT (Am^2/kg)	M_s at 5 K (Am^2/kg)	H_c at RT (mT)	H_c at 5 K (mT)	M_r/M_s at RT	M_r/M_s at 5 K	K_{eff} at 5 K (kJ/m^3)	K_{eff} at 300 K (kJ/m^3)
A	23 (2)	23 (1)	85 (2)	96 (2)	0.9 (2)	43.6 (2)	0.1	0.49	24.0 (5)	13.5 (5)
B	29 (3)	28 (1)	90 (2)	98 (2)	5.2 (2)	52.3 (2)	0.26	0.49	27.5 (5)	11.0 (5)

[a]Obtained by TEM (D_{TEM}), size of the crystalline domain (D_{XRD}) by Scherrer calculation, saturation magnetization (M_S) at RT and 5 K, coercivity (H_c) at RT and 5 K, reduced remanence at RT and 5 K and effective anisotropy constant (K_{eff}) obtained from the simulations of DC loops at 5 K and AC loops at 300 K.

https://dx.doi.org/10.1021/acsami.0c03222
ACS Appl. Mater. Interfaces 2020, 12, 27917−27929

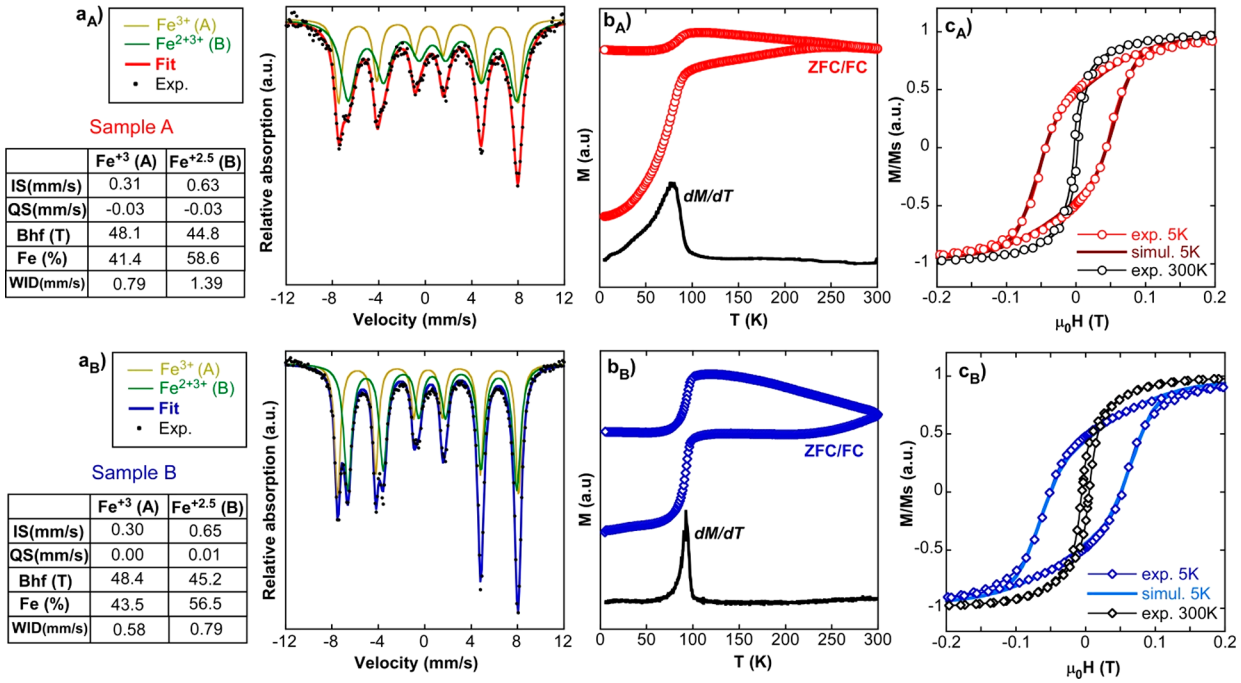

Sample A	Fe^{+3} (A)	$Fe^{+2.5}$ (B)
IS(mm/s)	0.31	0.63
QS(mm/s)	-0.03	-0.03
Bhf (T)	48.1	44.8
Fe (%)	41.4	58.6
WID(mm/s)	0.79	1.39

Sample B	Fe^{+3} (A)	$Fe^{+2.5}$ (B)
IS(mm/s)	0.30	0.65
QS(mm/s)	0.00	0.01
Bhf (T)	48.4	45.2
Fe (%)	43.5	56.5
WID(mm/s)	0.58	0.79

Figure 2. Magnetic characterization of samples A and B: (a) Mössbauer spectra, (b) ZFC/FC curves together with the derivative of ZFC magnetization, and (c) experimental hysteresis loops at 5 and 300 K together with a simulation at 5 K for single domains of 23 and 29 nm.

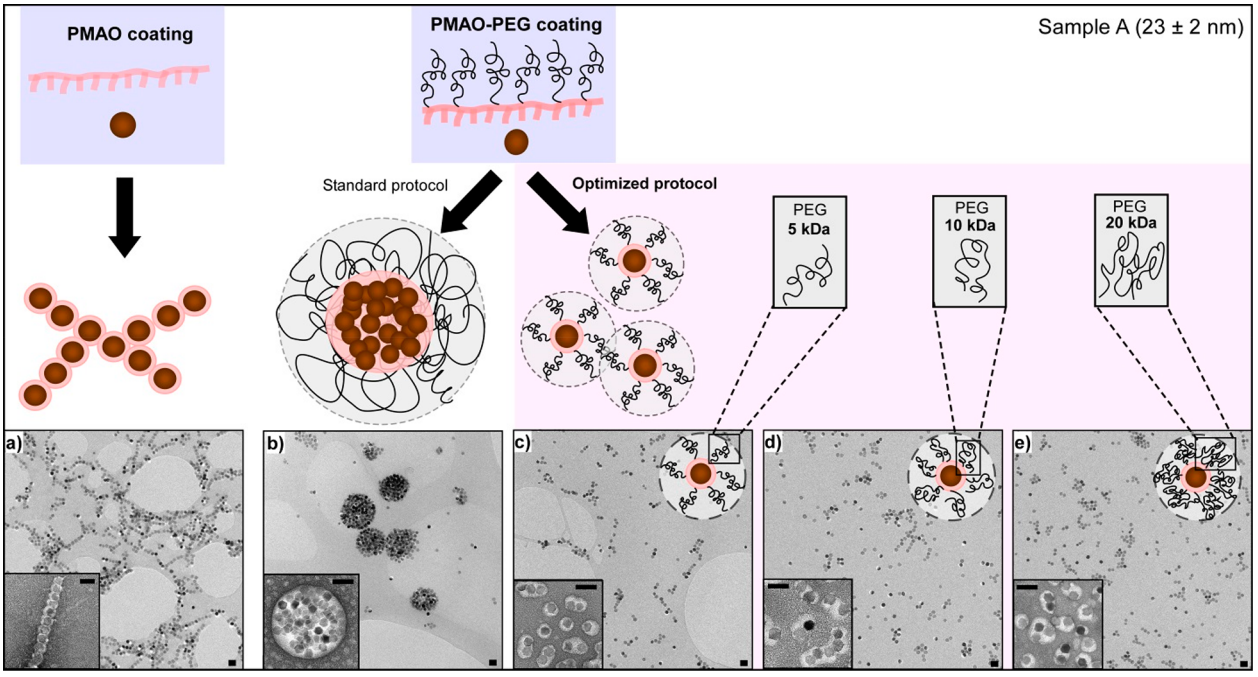

Figure 3. Configurations of sample A when wrapped with PMAO and PMAO−PEG. TEM micrographs of (a) A@PMAO, (b) A@PEG10k following the standard protocol, and (c) A@PEG5k, (d) A@PEG10k and (e) A@PEG20k following an optimized protocol. Insets: negative staining micrographs. Scale bars 50 nm.

PMAO−PEG coating protocol was optimized analyzing the effect of several parameters of the coating procedure (amount of monomers that is added per nm^2 of FM-NP surface, concentration, and solvent used in the initial FM-NPs colloids and PMAO−PEG solutions, timing, and so forth) on the aggregation degree of the FM-NPs (see Table S2, Table S3, and Figure S1 in Supporting Information). We found out that the addition order was critical to avoid large clusters; FM-NPs must be added dropwise into the PMAO−PEG solution in order to get individual or quasi-individual coatings. The optimized protocol leads to well-coated samples with the three PEGs (5, 10, and 20 kDa) in sample A, as can be observed in Figure 3c−e. The different polymer-wrapped structures (chains, clusters, and quasi-single NPs) are visible in the negative staining TEM micrographs of Figure 3. Analysis over the coating thickness of PEG 5, 10, and 20 kDa in the optimized protocol reveals that there is not a significant difference among them (Figure S2, Supporting Information).

https://dx.doi.org/10.1021/acsami.0c03222
ACS Appl. Mater. Interfaces 2020, 12, 27917−27929

Additionally, good colloidal stability was observed for sample A with the three PEG coatings, which also showed similar hydrodynamic diameters (D_h) (see Table S2, Supporting Information).

The FM-NPs of sample B (29 nm) were also coated following the optimized protocol, but in this case the three PEGs did not turned out equally successful. We observed that the colloidal stability of sample B decreased dramatically when the PEG used had a molecular weight of 5 or 10 kDa (see Figure 4 and Table S2). On the contrary, sample B@PEG20k exhibited good colloidal stability in both distillate water and physiological solution, presenting a D_h comparable to A@PEG (5, 10, 20k) (Table S2). The results obtained on this set of samples could be explained as due to the formation of more densely packed polymeric shells when the M_W of the PEG increases (see drawing scheme of Figures 3 and 4). Since larger FM-NPs present higher magnetic moments, it seems reasonable to infer that in the case of sample B more dense polymeric coatings are required to counteract the dipolar interactions.

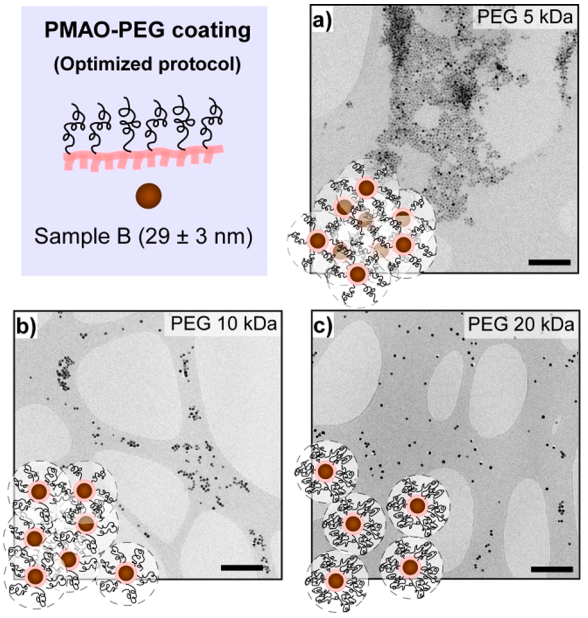

Figure 4. TEM micrographs of (a) B@PEG5k, (b) B@PEG10k, and (c) B@PEG20k obtained by the optimized protocol. Scale bars: 500 nm.

With the purpose of gaining a better understanding on how the density of the polymeric coating can affect the steric repulsive forces among FM-NPs, the particle−particle potential energy (V_{total}) in colloidal suspension was calculated based on the DLVO model[36,37] using available experimental data (see details in Model S1, Supporting Information). The output of the calculations for samples A@PEG (5, 10, 20k) and B@PEG20k shows soft asymmetric potential wells with a predominant repulsive character, whereas samples B@PEG (5, 10k) give rise to an almost purely attractive potential energy where the steric contribution is negligible (see Table S4 and Figure S3, Supporting Information). These results are consistent with the experimental observation and support the reasoning about the formation of polymeric coatings with similar thickness and increasing density as the PEG M_W becomes larger.

Hyperthermia Performance of FM-NPs in Several Configurations and Different Media. The configuration that FM-NPs adopt after polymer coating is entirely relevant to the heating performance of the system. So as to analyze the heating capacity of chains, clusters, and quasi-single NPs, the dynamic magnetization of samples A and B was measured by AMF magnetometry with field intensities ($\mu_o H_{ac}$) ranging from 0 to 40 mT. These measurements allow for determination of the specific absorption rate (SAR) by computing the area (A) of the hysteresis loops, according to eq 1

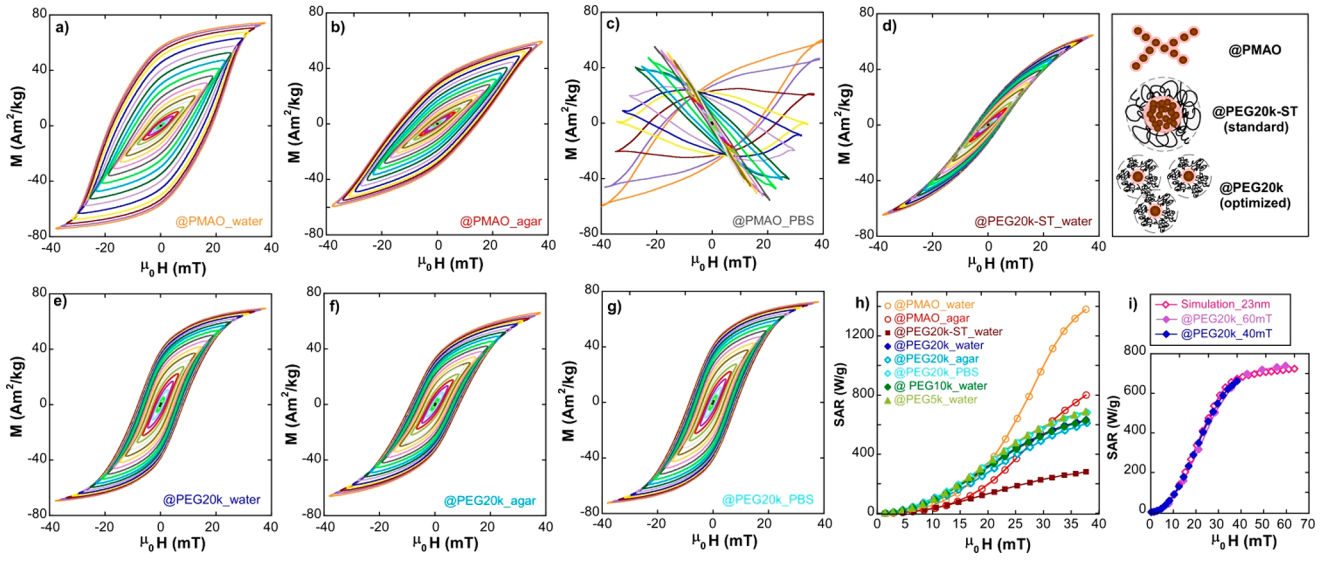

Figure 5. AC hysteresis loops of (a) A@PMAO in D.I. water, (b) A@PMAO in agar, (c) A@PMAO in PBS, (d) A@PEG20k-ST in D.I. water, (e) A@PEG20k in D.I. water, (f) A@PEG20k in agar, and (g) A@PEG20k in PBS. (h) Experimental SAR versus field curves corresponding to (a−g) AC loops and (i) experimental SAR versus field curves of A@PEG20k until 40 and 60 mT together with a simulated SAR versus field curve for FM-NPs of 23 nm. All measurements and simulations have been performed at 300 kHz and 300 K. Measurements up to 40 mT have been carried out by AC Magnetometer-1 and up to 60 mT by AC Magnetometer-2 (see Materials and Methods).

https://dx.doi.org/10.1021/acsami.0c03222
ACS Appl. Mater. Interfaces 2020, 12, 27917−27929

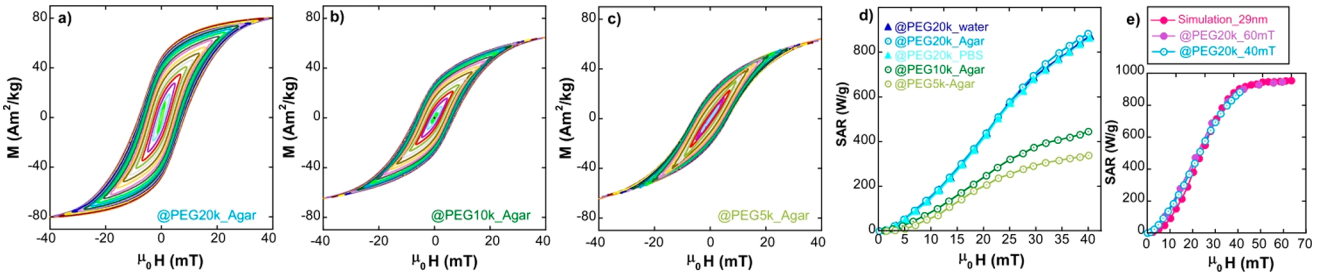

Figure 6. AC hysteresis loops of (a) B@PEG20k in agar (b) B@PEG10k in agar, (c) B@PEG5k in agar. (d) Experimental SAR versus field curves corresponding to (a−c) AC loops and (e) experimental SAR versus field curves of B@PEG20k until 40 and 60 mT together with a simulated SAR versus field curve for FM-NPs of 29 nm. All measurements and simulations have been performed at 300 kHz and 300 K. Measurements up to 40 mT have been carried out by AC Magnetometer-1 and up to 60 mT by AC Magnetometer-2 (see Materials and Methods).

$$\mathrm{SAR}(W/g) = \frac{f}{c}A = \frac{f}{c}\oint \mu_0 M_t dH_t \quad (1)$$

In eq 1, M_t is the magnetization at time t, H_t is the sinusoidal magnetic field of frequency f at time t, and c is the iron oxide weight concentration in the dispersing medium, which was close to 0.5 mg/mL in all cases.

Figure 5 displays dynamical hysteresis loops of sample A, coated by PMAO (@PMAO) and PMAO−PEG (@PEG), in environments with different viscosities (agar % 2) and ionic strengths (PBS 1×). As can be observed in Figure 5a−c, PMAO coating produces highly variable outcome depending on the media where the FM-NPs are dispersed. In D.I. water (Figure 5a), hysteresis loops become strikingly "squared", with remanence significantly larger than 0.5 × M_S. The explanation of this relies on the ability of FM-NPs@PMAO to form chains in order to reduce the magnetostatic energy of the assembly. These chains of different lengths (see Figure 3a) are able to easily align toward the external AC field, in a similar way to magnetotactic bacteria.[38] This alignment process amplifies notably the hysteresis area A (and the SAR, yellow curve of Figure 5h) because the effective easy axes of the chains turn out to be collinear with the external AC field, a geometrical correlation that produces the highest hysteresis area. Obviously, if these chains become immobilized, the orientation effect disappears and hysteresis loops of chained particles "recover" the form of the random orientation case, in accordance with what is observed in Figure 5b, where the sample is in agar media. Therefore, the whole SAR versus field curve in agar (red colored, Figure 5h) is scaled down relative to the liquid sample by a factor of ∼0.6. In this regard, it is important to note that the chaining and alignment processes in real biological environments are very unlikely to happen, so they are not practical from the viewpoint of clinical applicability. Additionally, measurements presented in Figure 5c show the complete washout obtained when sampleA@PMAO NPs are dispersed in physiological conditions and become extremely unstable. This instability is caused by the screening of the surface negative charge of A@PMAO formulation by the ions of the physiological saline solution; consequently, the electrostatic repulsion among FM-NPs disappears and they rapidly agglomerate and precipitate.

On the other hand, Figure 5d shows the result of moderate clustering when the standard coating protocol with PMAO−PEG is used and colloidally stable clusters are formed by tens to hundreds of closely packed FM-NPs. In this case, the very significant dipolar interactions between particles drive the AC loops to "tilt" and to reduce notably the hysteresis (and the SAR) (garnet-colored curved of Figure 5h). On the contrary, the improved coating protocol gives rise to quasi-single FM-NP@PEG formulations that are able to prevent NP agglomeration and to keep their physical configuration practically unchangeable in very different environments. In this way, the dynamical hysteresis loops of optimized sampleA@PEG20k in D.I. H_2O, agar, and PBS, presented in Figures 5e−g, are highly similar, and thus curves of SAR versus field amplitude closely collapse in a single curve with a maximum SAR between 600 and 700 W/g at 40 mT and 300 kHz. We also found out that the areas of the hysteresis loops of sample A for @PEG20k, 10k and 5k were equivalent and in the three cases magnetization dynamic stayed unalterable when the viscosity or the ionic strength of the media was changed (see Figure 5h and Figure S5 in Supporting Information)

In any case, the shape of all the SAR(H) curves (Figure 5h) showed a clear tendency of saturation at the highest field amplitude reached in these experiments (40 mT). It is well-known that the area of the hysteresis loops of FM-NPs, whose sizes are sufficiently large, follows a step pattern; it is quite small in the low field range and tends to saturate quite fast at high fields above a certain threshold value. In practice, the step is usually smoothed due to the averaging effect brought about by the size and/or effective anisotropy distributions, and therefore the saturation region is sometimes outside the experimental limits. However, the determination of the SAR saturation level is important for simulation purposes, because such a level is strongly correlated with the effective anisotropy constant and the magnetic particle size.[39] With the aim of expanding the experimental results to the high field region, the dynamical hysteresis loops of A@PEG20k have been obtained up to a maximum field of 60 mT at 300 kHz in a different device (see AC Magnetometer-2 in Materials and Methods).[40] These data (purple-filled diamonds in Figure 5i), confirm that the SAR saturates in the region above 40 mT and, importantly, allows to obtain more reliably the average effective anisotropy constant of the FM-NPs at RT. This has been done by using the same approach based on the Stoner−Wohlfart model as that used to simulate DC magnetization loops at 5 K (see Figure 2c). The calculation follows entirely the model proposed by Carrey et al.[39] (more details in Model S2, Supporting Information) and the best fit is obtained with single domains of 23 nm, an average effective anisotropy of 13.5 kJ/m^3, and the same standard deviation as that found in DC low temperature loops (dev = 5 kJ/m^3) (see Figure S6 in Supporting Information).

When the size of the FM-NPs increases (≥29 nm) as in sample B, PEGs with higher molecular weight (≥20 kDa) are necessary to keep the magnetic cores far enough and to

https://dx.doi.org/10.1021/acsami.0c03222
ACS Appl. Mater. Interfaces 2020, 12, 27917−27929

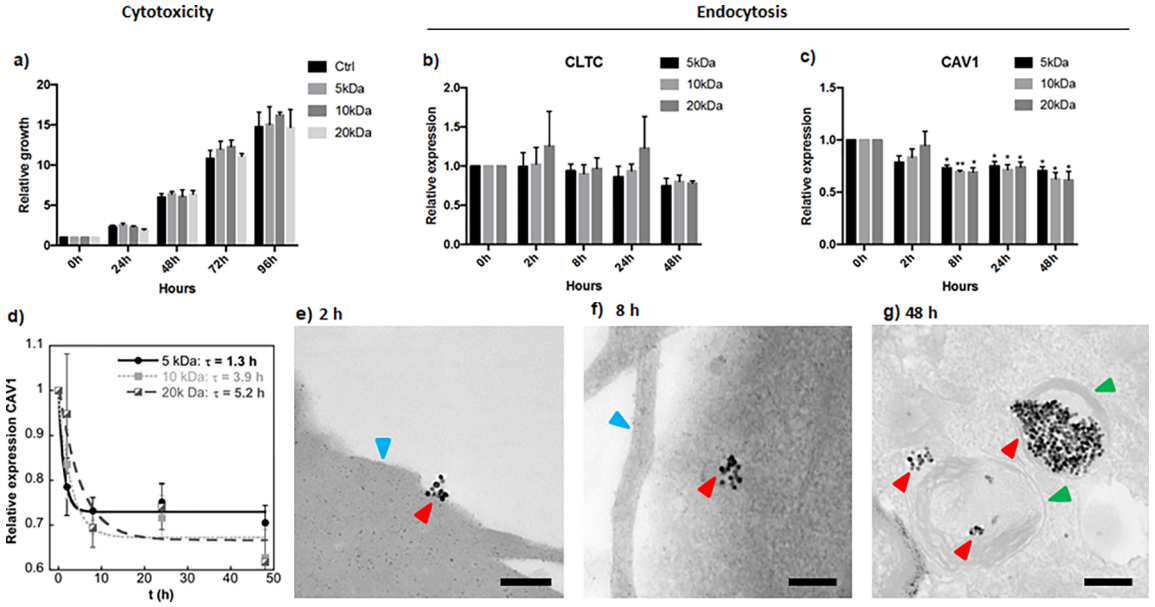

Figure 7. (a) Cytotoxicity assay of cells incubated with sampleA@PEG (5, 10, and 20 kDa) at different time points. Growth rates were plotted as relative increase compared to 0 h. Values are represented as the mean and standard error of the mean of three independent experiments. Gene expression analysis of (b) *CLTC* and (c) *CAV1* in cells incubated with sampleA@PEG (5, 10, and 20 kDa) at different time points. Expression was calculated relative to the housekeeping gene RPLP0 and values were plotted as relative changes compared to 0 h. Values are represented as the mean and standard error of the mean of three independent experiments. $*p < 0{,}05$, $**p < 0{,}01$; paired Student's *t* test. (d) Cellular uptake kinetics of sampleA@PEG (5, 10, and 20 kDa) based on *CAV1* gene expression, the uptake mean-life is calculated by curve fitting using an exponential function. Representative TEM images corresponding to incubation times of (e) 2, (f) 8, and (g) 48 h. Arrowheads: red, FM-NPs; blue, cell surface; and green, endosome. Scale bars 200 nm.

prevent aggregation and/or colloidal instabilities. The progressive tilting and hysteresis reduction in the plots of Figure 6a–c clearly reflect the gradual influence of increasing interparticle interactions when the coating density is reduced (from PEG of 20 to 5 kDa), with the concomitant drop of SAR from the peak level of 850 W/g (PEG of 20 kDa) to 350 W/g (PEG of 5 kDa), as shown in Figure 6d.

The study has been completed by expanding the range of experimental field amplitudes up to 60 mT, exactly as done in sample A. It is also observed (see Figure 6e) that the SAR saturates above 40 mT but at a higher level than in sample A (850 W/g against 650 W/g approximately), which can be undoubtedly related to the larger particle size of sample B. SAR(H) curve is reasonably simulated in the same framework as used for sample A, by considering magnetic single domains of 29 nm with an average effective anisotropy constant at RT of 11 kJ/m^3.

***In vitro* Analysis of FM-NP@PEG Formulation.** After verifying that with an optimized PEG coating neither samples A nor B changed their heating power in such different media as D.I. water, agar, or physiological saline solution, several *in vitro* experiments in the colon cancer-derived cell line HCT116 were carried out. Since the three optimized formulations of sample-A@PEG (5, 10, and 20 kDa) had proven to have an equivalent colloidal stability and heating efficiency, we used these samples to perform cytotoxicity and endocytosis studies, and to analyze the role of PEG length on the cellular dynamics.

First of all, we studied the cytotoxicity of sample-A@PEG (5, 10, and 20 kDa) at different time points ranging from 0 to 96 h. Figure 7a shows that cells incubated with sample-A@PEG (5, 10, and 20 kDa) grow at the same rate as control cells with no significant differences between the three PEGs; thus, it can be concluded that these FM-NP formulations are not toxic for the cells.

Assessment of endocytosis time frame was done using gene expression analysis and TEM study. Incubation of cells with nanoparticles showed a significant decrease of *CAV1* gene expression after 8 h and no changes in the expression of *CLTC* (see Figure 7b,c). These genes take part in the caveolae- and chlatrin-mediated endocytosis processes, respectively. *CAV1* regulates the endocytic pathway by slowing down the internalization of caveolae, and it has been shown that cells lacking *CAV1* have a rapid endocytosis transit.[41] Our results suggest that incubation of cells with nanoparticles accelerates the caveolae-mediated endocytosis pathway. These results are in accordance with previous studies where nanoparticles utilize nonclathrin-mediated endocytosis for uptake, entering selectively in caveolae.[42] Additionally, it has been reported that caveolae-mediated endocytosis is more prominent in endothelial cells than in other cell types.[43] In order to compare the kinetic differences in cellular uptake for PEG coatings of 5, 10, and 20 kDa, the relative gene expression of *CAV1* was plotted as a function of incubation time and fitted to a single exponential function. Figure 7d shows that the uptake of A@PEG samples follows a characteristic time-dependent profile in which the uptake rate increases fast at first and gradually slows down to reach a plateau at 7–24 h, depending on the molecular weight of the PEG. The uptake mean-life (τ) determined by the exponential fitting for the three PEG coatings (5, 10, and 20 kDa) was 1.3, 2.9, and 5.2 h, respectively. These results clearly show that the uptake of the NPs is significantly reduced when the molecular weight of the PEG used in the coating is higher. A τ-value of 5.2 h is quite high in comparison with the values reported in other NP systems.[44−47] This relatively large endocytosis resistance is

https://dx.doi.org/10.1021/acsami.0c03222
ACS Appl. Mater. Interfaces 2020, 12, 27917−27929

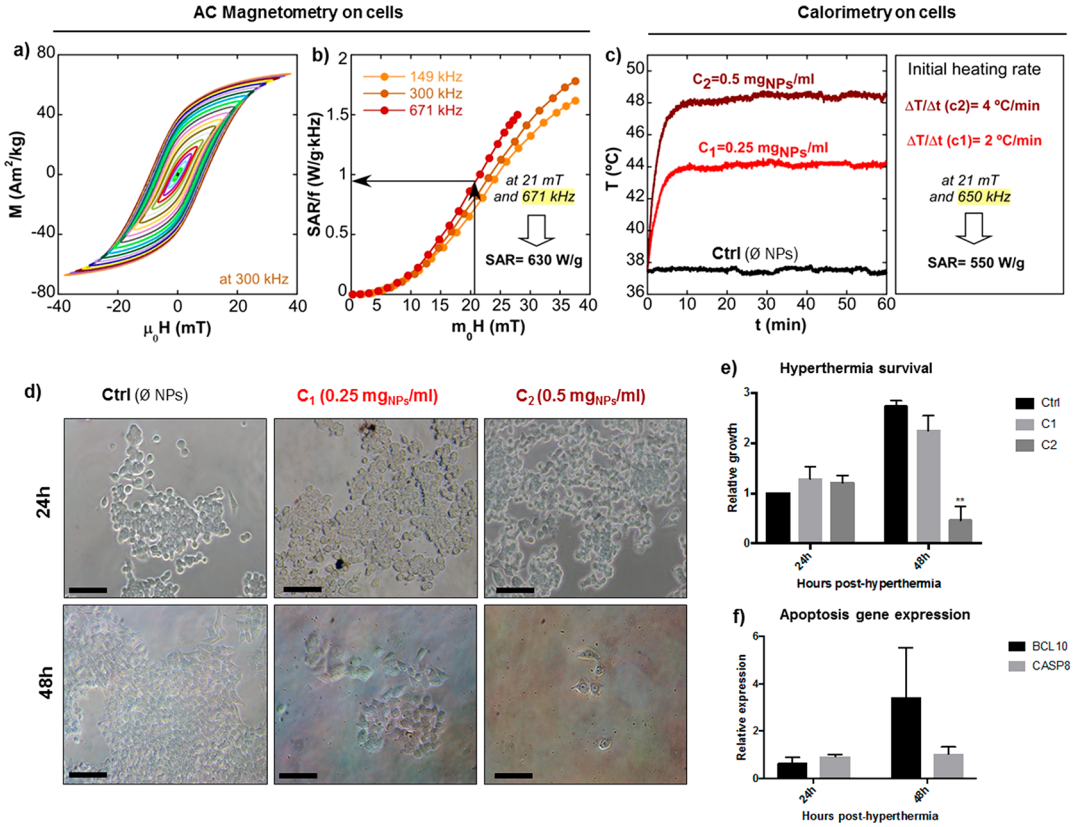

Figure 8. Magnetic hyperthermia on colon cancer-derived cell line HCT116. (a) AC hysteresis loops of A@PEG20k in cell culture at 300 kHz. (b) Experimental SAR versus field curves of A@PEG20k at 149, 300, and 671 kHz. (c) Calorimetric measurements *in vitro* and calculated SAR for initial slope. AC Magnetometry on cells have been performed by AC Magnetometer-1, calorimetry on cells and hyperthermia treatment *in vitro* have been carried out by a homemade electromagnetic applicator (see Materials and Methods). (d) Representative optical micrographs taken at 24 and 48 h posthyperthermia for the different nanoparticle concentrations used (C_1 = 0.25 mg_{NPs}/ml and C_2 = 0.5 mg_{NPs}/ml), scale bars 100 μm. (e) Hyperthermia survival was quantified by plotting the relative growth of cells 24 and 48 h posthyperthermia treatment. Growth rates were plotted as relative values compared to the 24 h control (water). (f) Gene expression analysis of apoptotic genes *BCL10* and *CASP8* in cells incubated with C1 and exposed to magnetic field. RNA was extracted from the cells after incubation for 24 and 48 h posthyperthermia. Expression was calculated relative to the housekeeping gene RPLP0. Values are represented as the mean and standard error of the mean of three independent experiments. $^{**}p < 0{,}01$; paired Student's *t* test.

advantageous to perform the hyperthermia treatment in a pre-endocytosis stage. In this stage, it can be ensured that the therapy is taking place prior to the intracellular biodegradation of the FM-NPs; thus, the SAR is not affected by the chemical changes that the inorganic cores will undergo inside the cell until their complete dissolution.

Additionally, the cellular localization of the NPs of sampleA@PEG-20k was investigated by TEM analysis. The corresponding examination of the micrographs revealed that nanoparticles are not found inside the cells at 2 h (Figure 7e). After 8 h of incubation time, small groups of NPs start to be found in endosomal compartments in the proximity of the plasma membrane (Figure 7f). Finally at 48 h, large amounts of FM-NPs are visible within the cytoplasm and further away from the cell periphery (Figure 7g). These results are in total agreement with the *CAV1* gene expression analysis, where after 8 h incubation a significant reduction of *CAV1* was observed.

To perform magnetic hyperthermia experiments *in vitro*, we chose the sample with the highest resistance to endocytosis (A@PEG-20k). These hyperthermia experiments required larger application volume to accommodate the cell culture wells, so they were conducted using a homemade electromagnetic applicator with a solenoid coil of larger dimensions (see Materials and Methods) that is capable of delivering a maximum field of 21 mT at 650 kHz. In this device, the SAR of the cell cultures was determined by calorimetry technique. Since the AMF conditions herein are different to those employed in the measurements of the dynamical hysteresis loops in the previous section (maximum field amplitude of 40 mT at 300 kHz by AC Magnetometer-1), the hysteresis loops of sampleA@PEG-20k within cell culture were obtained at three different frequencies (149, 300, and 671 kHz) for clearer comparison. The hysteresis loops obtained within cell culture at 300 kHz, presented in Figure 8a, result to be practically identical to the measurements of sampleA@PEG-20 kDa in D.I. water, agar, and PBS (Figure 5e–g). Thus, it can be inferred that the heating efficiency of A@PEG-20 kDa does not decrease during *in vitro* conditions either. However, the frequency-normalized SAR (SAR/f) versus field amplitude curves, shown in Figure 8b, are not superimposed to each other; in other words, the hysteresis area is slightly frequency-dependent. This was expected for particles of 23 nm given that the Stoner–Wohlfart-based models predict this behavior (as shown in Figure S7, Supporting Information), which ultimately means that thermal fluctuations at room temperature in sample A are not negligible. This being so, the intrinsic heat production obtained from AC magnetometry at 671 kHz and 21 mT is around 630 W/g (Figure 8b). As mentioned above,

https://dx.doi.org/10.1021/acsami.0c03222
ACS Appl. Mater. Interfaces 2020, 12, 27917–27929

the hyperthermia treatment *in vitro* was performed using an electromagnetic applicator at 21 mT and 650 kHz for 1 h while measuring the temperature as a function of time. As the total incubation time of cells with NPs was less than 2 h, it can be stated that the hyperthermia treatment was performed prior to endocytosis. Two different NP concentrations were used (C_1 = 0.25 and C_2 = 0.5 mg/mL) and the determined initial heating rates were 2 and 4 °C/min, respectively (see Figure 8c). The cells with A@PEG-20 kDa reached 44 °C (for C_1) and 48 °C (for C_2), while the control stayed at the T of the background (37 °C). The determined SAR value from calorimetry experiments is around 550 W/g, which is in good accord with the value obtained from AC magnetometry at 21 mT and 671 kHz, proving, again, the good reproducibility and reliability of this FM-NP@PEG formulation.

The optic micrographs in Figure 8d show cell cultures at 24 and 48 h posthyperthermia. After 24 h, no differences in the number of cells quantified by crystal violet staining were observed (Figure 8e), although cells incubated with higher concentration of nanoparticles presented altered morphology. At 48 h posthyperthermia, a dramatic decrease in the number of cells was observed in the wells with higher FM-NP concentration (C_2) (see Figure 8d,e). Although the reduction of cell number for the lower FM-NP concentration (C_1) was not statistically significant, an increase in expression of apoptotic genes *BCL10* and *CASP8* was observed (Figure 8f), pointing to an activation of the apoptotic process that would eventually lead to cell death.

CONCLUSIONS

In this work, we present an optimized coating protocol of magnetite NPs (large enough to have permanent magnetization: Sample A = 23 nm and Sample B = 29 nm) with PEG molecules of high molecular weight (5−20 kDa). This improved polymeric coating method, by which FM-NPs become individually or quasi-individually coated, is able to counterbalance the dipolar interparticle interactions that are particularly strong among large MNPs. Larger FM-NPs (29 nm) require longer PEG molecules (20 kDa) to keep the magnetic cores far enough from each other. These FM-NPs@PEG systems maintain the low NP aggregation level within environments of different ionic strengths and viscosities. In this way, the high heating efficiency of the FM-NP@PEG formulations has been shown to stay invariable in such diverse media as distilled water, physiological saline solution, agar, and cell culture. The great reproducibility and reliability of the heating performance of these optimized FM-NP@PEG systems is an important achievement as it solves the variability and unpredictability that nanoparticle-mediated magnetic hyperthermia has presented to date. The magnetothermal response of the FM-NP@PEG samples have been measured using two AC magnetometers that reach different maximum fields and by calorimetric technique, which leads to very consistent and compatible results.

In vitro experiments based on gene expression alterations performed into a colon cancer-derived cell line show that the uptake of the FM-NPs is mediated by caveolae-related mechanisms and not through clatrhin-mediated endocytosis. It has been observed that the higher the molecular weight of the PEG, the more resistant to endocytosis the FM-NP@PEG system becomes. SampleA@PEG20 kDa presents a relatively large uptake mean-lifetime in comparison with other NP systems (τ = 5.2 h). Moreover, this sample has been used successfully for hyperthermia treatment *in vitro*, where a treatment of 60 min at 21 mT and 650 kHz in a pre-endocytosis stage causes complete cell death at 48 h posthyperthermia. These unprecedented advances in the reproducibility and predictability of the heating power of MNPs within cell environment open up promising opportunities in the development of next-generation medical technologies.

MATERIALS AND METHODS

Materials. Iron(III) chloride hexahydrate was purchased from Across (99%), sodium oleate from TCI America (97%), poly(ethylene glycol)-amine (PEG-NH_2) from Laysan Bio (M_W = 5000−20 000 Da), ethanol from Panreac S.A, and phosphate-buffered saline (PBS) from Gibco. All other solvents and reagents were purchased from Sigma-Aldrich and used as received without purification: oleic acid (90%), 1-octadecene (ODE) (90%), dibenzyl ether (DBE) (98%), hexane (99%), and poly(maleic anhydride-*alt*-1-octadecene) (PMAO) (M_W = 30 000−50 000 Da).

Synthesis of FM-NPs of Fe_3O_4. The following procedure was used to obtain cuboctahedral single crystals of magnetite:

Briefly, 5 mmol of iron(III) oleate was dissolved in a 2:1 mixture of organic solvents (10 mL of 1-octadecene + 5 mL of dibenzyl ether) together with oleic acid (12 mmol). The mixture was heated in 2 steps under N_2 (g). First, at 10 °C/min from RT to 200 °C and, second, at 3 °C/min from 200 to 315 °C (to obtain 23 nm NPs, sample A) or to 320 °C (to obtain 29 nm NPs, sample B). The final T was kept for 30 min and then the product was cooled to RT. The entire synthesis was carried out under mechanical stirring (at 120 rpm). The final product was cleaned by centrifugation (20 000 rpm) using THF, EtOH, and hexane as explained in our previous work.[21] The stock solution was dispersed in $CHCl_3$ and stored in the fridge.

PMAO and PMAO−PEG Polymer Coatings. The amphiphilic copolymer (PMAO-grafted-PEG) was previously synthesized by binding long poly(ethylene glycol)-amine (PEG-NH_2) tales (5−20 kDa) in a high density into the poly(maleic anhydride-*alt*-1-octadecene) PMAO backbone, specifically 75% of PMAO monomers are used in the grafting reaction. The standard procedure used to coat the FM-NPs with PMAO or PMAO-*g*-PEG was carried out based on the procedure described elsewhere.[48] In order to get the FM-NPs individually or quasi-individually coated, the procedure was modified by a systematic study of several parameters. The protocol was refined through the analysis of the dynamical hysteresis loops and SAR values of different preparations in which one parameter was changed at a time (Table S3 and Figure S1 in Supporting Information). Briefly, in an optimized protocol the stock solution of FM-NPs in $CHCl_3$ ($c \sim$ 20 mg/mL) is added dropwise to the PMAO−PEG solution in $CHCl_3$ ($c \sim 5\ mg_{PMAO}/ml$) using 50 monomers of PMAO per nm^2 of NP surface. The mixture is stirred for 30 min, and the solvent is evaporated in a rotavapor. Finally, the hydrolysis of the remaining maleic anhydride groups in the polymeric surface is completed by adding sodium borate buffer at pH = 9. The Z potential and the hydrodynamic radius of the samples presented in the article are summarized in Table S2, Supporting Information.

Physical, Structural, and Magnetic Experimental Details. X-ray diffraction (XRD) patterns of the as-synthesized dried samples were obtained using a PANalytical X'Pert PRO diffractometer equipped with copper anode (operated at 40 kV and 40 mA), diffracted beam monochromato,r and PIXcel detector. Scans were collected in the 10−90° 2θ range with step size of 0.02° and scan step speed of 1.25 s.

The percentage of organic matter in as-synthesized hydrophobic NPs was determined by thermogravimetric measurements, performed in a NETZSCH STA 449 C thermogravimetric analyzer, by heating 10 mg of sample at 10 °C/min under dry Ar atmosphere (see Figure S8, Supporting Information).

Dynamic light scattering (DLS) and ζ-potential of the NPs coated with PMAO and PMAO-*g*-PEG were analyzed using a Zetasizer Nano-ZS (Malvern Instruments).

https://dx.doi.org/10.1021/acsami.0c03222
ACS Appl. Mater. Interfaces 2020, 12, 27917−27929

TEM micrographs of both, as-synthesized and water-stable NPs with PMAO and PMAO−PEG, were obtained using a JEOL JEM 2010 with an accelerating voltage of 200 kV, and a point resolution of 0.19 nm, which provides morphology images and the corresponding crystal structures by selected-area electron diffraction. For the measurements of water-stable NPs, the surface of TEM grids were made hydrophilic by low-vacuum glow discharge at about 8000 V for 30 s.

For negative staining, nanoparticles were negatively stained by first diluting them to a concentration of about 4 μg/mL in distilled water. A copper grid with attached thin carbon film (100−150A), which had been subjected to a low-vacuum glow discharge at about 8000 V for 30 s, was floated on the surface of the nanoparticles suspension. The grid was then transferred to the surface of the staining solution (1% uranyl acetate). The grid was removed after 1−2 min and excess stain was removed by touching the edge with a piece of filter paper.

Mössbauer spectroscopic studies were performed in as-synthesized dried samples using a constant acceleration spectrometer with a 57CoRh source. Velocity calibration was carried out by using a metallic Fe foil, and the Mössbauer spectra parameters are given relative to this standard at room temperature. The spectra were fitted with the NORMOS program.

Quasi-static magnetization measurements as a function of magnetic field, $M(H)$ and temperature $M(T)$ were carried out using a SQUID magnetometer (MPMS3, Quantum design). These measurements were performed by drying aqueous colloids of PMAO coated NPs (~0.1 mg/mL) on semipermeable filter paper. The saturation magnetization, M_s, at RT and 5 K were obtained from dried as-synthesized samples (powder) and normalized per unit mass of inorganic matter by subtracting the weight percentage of organic matter determined by thermogravimetry.

AC Magnetometer-1 (9 turns coil, 6.75 cm in length, and 2.5 cm internal-diameter). Most hyperthermia measurements have been performed by alternating magnetic field (AMF) magnetometry in a homemade device previously described by Garaio et al.[49] Briefly, it consists of an air−core inductor part of a resonant circuit fed by a power amplifier. The dynamic magnetization, $M(t)$, is obtained by a pick-up coil system composed of two coils wound in opposite directions. These measurements have been carried out in PMAO and PMAO−PEG coated NPs dispersed in distilled water, PBS (1×, pH = 7.4) and Agar (2%) with a mass concentration $c \sim 0.3$ mg/mL in a solution volume of 1−1.5 mL. The dynamic hysteresis loops were measured at room temperature (25 °C) at selected frequencies of 149, 302, and 671 kHz, and with an applied magnetic field ranging from 0 to 40 mT.

AC Magnetometer-2 (12 turns coil, 4.1 cm in length and 1.2 cm internal-diameter). High-field hyperthermia measurements have been done using a homemade AC magnetometer that generates high magnetic field able to saturate the samples.[40] This device is capable of working at a wide frequency range (100−950 kHz) with large field intensities: up to 90 mT at low frequencies and up to 31 mT at high frequencies. Since in this device the working volume is smaller, the NPs colloids are placed in 100 μL container; to reach similar accuracy as AC Magnetometer-1, the samples are concentrated up to 1.2 mg/mL. The dynamic hysteresis loops were measured at 300 kHz frequency and field intensity ranging from 0 to 60 mT in order to compare the results with those obtained in AC Magnetometer-1.

Hyperthermia treatment *in vitro* was performed using a homemade electromagnetic applicator (9 turns coil, 8.1 cm in length and 6.5 cm internal-diameter) with a larger working volume that allows placing cell culture wells within the solenoid. The AC magnetic field was generated using a solenoid coil that is part of an LCC resonant circuit fed by a 2 kW power amplifier. During the hyperthermia treatment, the cells (6 wells from 96-well plate) were placed within the homogeneous area of the coil.

The units (mg/mL, A·m^2/kg, and W/g) given throughout the paper are normalized to the mass of inorganic matter.

***In Vitro* Study.** *Cell Culture.* The human colorectal cancer cell line HCT116 (ATCC) was cultured in Dulbecco's Modified Eagle Medium (DMEM) (Gibco) and supplemented with 10% FBS and antibiotics. Cells were grown at 37 °C and 5% CO_2 atmosphere.

RNA Extraction, Reverse Transcription, and qPCR. Total RNA was extracted from cells using a commercial RNA extraction kit (Machinery Nagel). All samples were subjected to DNase I treatment. Ten nanograms of RNA were used for reverse transcription (RT) and real-time quantitative PCR (qPCR) using iTaq Universal SYBR One-Step Kit (BioRad). The amplified transcripts were quantified using the comparative cycle threshold method. All primer sequences are available upon request.

Cytotoxicity Assay. Cells were seeded in 96-well plates at a density of 1200 cells per well. Cells were allowed to attach to the plate before adding nanoparticles (10 μg of NPs were added per well). Proliferation was measured at days 0, 1, 2, 3, and 4. For crystal violet staining, cells were fixed in 4% paraformaldehyde and stained with 0.1% crystal violet. After staining, cells were washed and 10% acetic acid was added. Absorbance was measured at 590 nm.

Endocytosis. For the analysis of endocytosis-related gene expression, cells were incubated in 24-well plates (at a density of 5 × 10^4 cells and 5 μg of NPs per well) for 2 h, 8 and 48 h. After incubation, cells were harvested, RNA was extracted, and gene expression was quantified as described above. Specific primers for *CAV1* and *CLTC* (involved in caveolar and chlatrin-mediated endocytosis, respectively) were used for RT-QCR experiments.

For TEM experiments, cells were seeded in 10 cm plates at a density of 5 × 10^6 cells per plate and were incubated with 0.5 mg nanoparticles per plate for 2, 8, and 48 h. After incubation, cells were prefixed with 0.5% glutaraldehyde for 15 min and centrifuged at 800 g for 10 min. Pellets were fixed with 2% glutaraldehyde overnight at 4 °C.

For embedding the samples and ultramicrotomy, cell pellets were washed in Sorenson's buffer (SB) with 6% sucrose and fixed in 2% glutaraldehyde for 1 h. Then, pellets were washed twice in SB and osmicated in 1% osmium tetroxide for 1 h. After washing in SB, pellets were dehydrated in graded acetone (50%, 70%, 96%, 100%) and embedded in Epon resin 812. Seventy nanometer ultrathin sections were collected on mesh nickel grids and examined in a JEOL JEM 1400 Plus electron microscope. Tissue preparations were photographed by using a digital camera coupled to the electron microscope.

Magnetic Hyperthermia In Vitro. A total of 5 × 10^6 cells were mixed with 0.5 mg of NPs and transferred to a glass vial to perform the dynamical hysteresis loops at NP concentration of 0.5 mg_{NP}/ml using the AC Magnetometer-1.

For the *in vitro* hyperthermia experiments 96-well plates with 6 × 10^3 cells per well in 100 μL media were used. These experiments were carried out using two NP concentrations (C_1 = 0.25 mg_{NP}/ml and C_2 = 0.5 mg_{NP}/ml). Hyperthermia treatments were performed at 21 mT and 650 kHz during 1 h in the homemade electromagnetic applicator described above, and the temperature of the background was kept at 37 °C. The temperature profile in the samples was monitored using a commercial nonresistive optical fiber (Opsens). Then cells were incubated for 24 and 48 h post-hyperthermia to see the effect of the treatment.

■ ASSOCIATED CONTENT

Supporting Information

The Supporting Information is available free of charge at https://pubs.acs.org/doi/10.1021/acsami.0c03222.

Crystalline sizes, DLS measurements, refinement of the coating protocol, polymeric coating thickness, theoretical modeling of colloidal stability, hysteresis loops simulation of DC and AC loops, frequency dependency of SAR and thermogravimetric measurements. (PDF)

https://dx.doi.org/10.1021/acsami.0c03222
ACS Appl. Mater. Interfaces 2020, 12, 27917−27929

AUTHOR INFORMATION

Corresponding Authors

Idoia Castellanos-Rubio − *Departamento de Química Inorgánica and Department of Electricidad y Electrónica, Facultad de Ciencia y Tecnología, UPV/EHU, 48940 Leioa, Spain;* orcid.org/0000-0003-4525-4883; Email: idoia.castellanos@ehu.eus

Maite Insausti − *Departamento de Química Inorgánica, Facultad de Ciencia y Tecnología, UPV/EHU, 48940 Leioa, Spain; BC Materials, Basque Center for Materials, Applications, and Nanostructures, 48940 Leioa, Spain;* Email: maite.insausti@ehu.eus

Authors

Irati Rodrigo − *Department of Electricidad y Electrónica, Facultad de Ciencia y Tecnología, UPV/EHU, 48940 Leioa, Spain; BC Materials, Basque Center for Materials, Applications, and Nanostructures, 48940 Leioa, Spain*

Ane Olazagoitia-Garmendia − *Departamento de Genética, Antropología Física y Fisiología Animal, Facultad de Medicina y Enfermería, 48940 Leioa, Spain; Biocruces Bizkaia Health Research Institute, 48903 Barakaldo, Spain*

Oihane Arriortua − *Departamento de Química Inorgánica, Facultad de Ciencia y Tecnología, UPV/EHU, 48940 Leioa, Spain*

Izaskun Gil de Muro − *Departamento de Química Inorgánica, Facultad de Ciencia y Tecnología, UPV/EHU, 48940 Leioa, Spain*

José S. Garitaonandia − *Departamento de Física Aplicada II, Facultad de Ciencia y Tecnología, UPV/EHU, 48940 Leioa, Spain*

Jose Ramón Bilbao − *Departamento de Genética, Antropología Física y Fisiología Animal, Facultad de Medicina y Enfermería, 48940 Leioa, Spain; Biocruces Bizkaia Health Research Institute, 48903 Barakaldo, Spain; Spanish Biomedical Research Center in Diabetes and Associated Metabolic Diseases (CIBERDEM), 28029 Madrid, Spain*

M. Luisa Fdez-Gubieda − *Department of Electricidad y Electrónica, Facultad de Ciencia y Tecnología, UPV/EHU, 48940 Leioa, Spain;* orcid.org/0000-0001-6076-7738

Fernando Plazaola − *Department of Electricidad y Electrónica, Facultad de Ciencia y Tecnología, UPV/EHU, 48940 Leioa, Spain*

Iñaki Orue − *SGIker, Servicios Generales de Investigación, UPV/EHU, 48940 Leioa, Spain*

Ainara Castellanos-Rubio − *Departamento de Genética, Antropología Física y Fisiología Animal, Facultad de Medicina y Enfermería, 48940 Leioa, Spain; Biocruces Bizkaia Health Research Institute, 48903 Barakaldo, Spain; Spanish Biomedical Research Center in Diabetes and Associated Metabolic Diseases (CIBERDEM), 28029 Madrid, Spain; IKERBASQUE Basque Foundation for Science, 48013 Bilbao, Spain*

Complete contact information is available at: https://pubs.acs.org/10.1021/acsami.0c03222

Notes

The authors declare no competing financial interest.

ACKNOWLEDGMENTS

This work was supported by institutional funding from the Basque Government under GU_IT1226-19 Project and from the Spanish Ministry of Economy and Competitivenes under MAT2019-106845RB Project. Dr. I. Castellanos-Rubio thanks the Horizon 2020 Programme for the financial support provided through a Marie Sklodowska-Curie fellowship (798830). The authors thank Dr. Alex Díez and Dr. Ricardo Andrade (Analytical and High-Resolution Microscopy in Biomedicine, UPV/EHU) for their assistance. The technical and human support provided by SGIker (UPV/EHU) is also gratefully acknowledged.

REFERENCES

(1) Pankhurst, Q. A.; Thanh, N. T. K.; Jones, S. K.; Dobson, J. Progress in Applications of Magnetic Nanoparticles in Biomedicine. *J. Phys. D: Appl. Phys.* **2009**, *42* (22), 224001.

(2) Xie, J.; Liu, G.; Eden, H. S.; Ai, H.; Chen, X. Surface-Engineered Magnetic Nanoparticle Platforms for Cancer Imaging and Therapy. *Acc. Chem. Res.* **2011**, *44* (10), 883−892.

(3) Du, Y.; Liu, X.; Liang, Q.; Liang, X.; Tian, J. Optimization and Design of Magnetic Ferrite Nanoparticles with Uniform Tumor Distribution for Highly Sensitive MRI/MPI Performance and Improved Magnetic Hyperthermia Therapy. *Nano Lett.* **2019**, *19*, 3618−3626.

(4) Torres-Lugo, M.; Rinaldi, C. Thermal Potentiation of Chemotherapy by Magnetic Nanoparticles R Eview. *Nanomedicine* **2013**, *8*, 1689−1707.

(5) Deatsch, A. E.; Evans, B. A. Journal of Magnetism and Magnetic Materials Heating Efficiency in Magnetic Nanoparticle Hyperthermia. *J. Magn. Magn. Mater.* **2014**, *354*, 163−172.

(6) Das, P.; Colombo, M.; Prosperi, D. Colloids and Surfaces B: Biointerfaces Recent Advances in Magnetic Fl Uid Hyperthermia for Cancer Therapy. *Colloids Surf., B* **2019**, *174*, 42−55.

(7) Wang, Y. J. Current Status of Superparamagnetic Iron Oxide Contrast Agents for Liver Magnetic Resonance Imaging. *World J. Gastroenterol.* **2015**, *21* (47), 13400−13402.

(8) Stark, W. J. Nanoparticles in Biological Systems Angewandte. *Angew. Chem., Int. Ed.* **2011**, *50*, 1242−1258.

(9) Xie, B. J.; Xu, C.; Kohler, N.; Hou, Y.; Sun, S. Controlled PEGylation of Monodisperse Fe3O4 Nanoparticles for Reduced Non-Specific Uptake by Macrophage Cells. *Adv. Mater.* **2007**, *19*, 3163.

(10) Li, S.-D.; Huang, L. Stealth Nanoparticles: High Density but Sheddable PEG Is a Key for Tumor Targeting. *J. Controlled Release* **2010**, *145* (3), 178−181.

(11) Peng, C.; Zheng, L.; Chen, Q.; Shen, M.; Guo, R.; Wang, H.; Cao, X.; Zhang, G.; Shi, X. Biomaterials PEGylated Dendrimer-Entrapped Gold Nanoparticles for in Vivo Blood Pool and Tumor Imaging by Computed Tomography. *Biomaterials* **2012**, *33*, 1107−1119.

(12) Duan, Z.; Cai, H.; Zhang, H.; Chen, K.; Li, N.; Xu, Z.; Gong, Q.; Luo, K. PEGylated Multistimuli-Responsive Dendritic Prodrug-Based Nanoscale System for Enhanced Anticancer Activity. *ACS Appl. Mater. Interfaces* **2018**, *10*, 35770−35783.

(13) Li, Y.; Kröger, M.; Kam Liu, W. Biomaterials Endocytosis of PEGylated Nanoparticles Accompanied by Structural and Free Energy Changes of the Grafted Polyethylene Glycol. *Biomaterials* **2014**, *35*, 8467−8478.

(14) Di Corato, R.; Espinosa, A.; Lartigue, L.; Tharaud, M.; Chat, S.; Pellegrino, T.; Menager, C.; Gazeau, F.; Wilhelm, C. Biomaterials Magnetic Hyperthermia Ef Fi Ciency in the Cellular Environment for Different Nanoparticle Designs. *Biomaterials* **2014**, *35*, 6400−6411.

(15) Plan Sangnier, A.; Van de Walle, A. B.; Curcio, A.; Le Borgne, R.; Motte, L.; Lalatonne, Y.; Wilhelm, C. On Their Long-Term Intracellular Biodegradation In. *Nanoscale* **2019**, *11*, 16488−16498.

(16) Cabrera, D.; Coene, A.; Leliaert, J.; Artes-Ibanez, E. J.; Dupre, L.; Telling, N. D.; Teran, F. J. Dynamical Magnetic Response of Iron Oxide Nanoparticles Inside Live Cells. *ACS Nano* **2018**, *12*, 2741−2752.

(17) Mejias, R.; Hernandez Flores, P.; Talelli, M.; Tajada-Herraiz, J. L.; Brollo, M. E. F.; Portilla, Y.; Morales, M. P.; Barber, D. F. Cell-

Promoted Nanoparticle Aggregation Decreases Nanoparticle-Induced Hyperthermia under an Alternating Magnetic Field Independently of Nanoparticle Coating, Core Size, and Subcellular Localization. *ACS Appl. Mater. Interfaces* **2019**, *11* (1), 340−355.
(18) Kobayashi, S.; Ohki, A.; Tanoue, M.; Inaoka, Y.; Murase, K. Comparative Study of Extracellular and Intracellular Magnetic Hyperthermia Treatments Using Magnetic Particle Imaging. *Open J. Appl. Sci.* **2017**, *07*, 647−660.
(19) Del Sol-Fernandez, S.; Portilla-Tundidor, Y.; Gutierrez, L.; Odio, O. F.; Reguera, E.; Barber, D. F.; Morales, M. P. Flower-like Mn-Doped Magnetic Nanoparticles Functionalized with Avβ3-Integrin-Ligand to Efficiently Induce Intracellular Heat after Alternating Magnetic Field Exposition, Triggering Glioma Cell Death. *ACS Appl. Mater. Interfaces* **2019**, *11* (30), 26648−26663.
(20) Ovejero, J. G.; Cabrera, D.; Carrey, J.; Valdivielso, T.; Salas, G.; Teran, F. J. Dipolar Interactions on the Magnetic Heating Efficiency of Iron Oxide Nanoparticles. *Phys. Chem. Chem. Phys.* **2016**, *18*, 10954−10963.
(21) Castellanos-Rubio, I.; Rodrigo, I.; Munshi, R.; Arriortua, O.; Garitaonandia, J. S.; Martinez-Amesti, A.; Plazaola, F.; Orue, I.; Pralle, A.; Insausti, M. Outstanding Heat Loss via Nano-Octahedra above 20 Nm in Size: From Wustite-Rich Nanoparticles to Magnetite Single-Crystals. *Nanoscale* **2019**, *11*, 16635−16649.
(22) Castellanos-Rubio, I.; Munshi, R.; Qin, Y.; Eason, D. B.; Orue, I.; Insausti, M.; Pralle, A. Multilayered Inorganic-Organic Microdisks as Ideal Carriers for High Magnetothermal Actuation: Assembling Ferrimagnetic Nanoparticles Devoid of Dipolar Interactions. *Nanoscale* **2018**, *10*, 21879−21892.
(23) Avugadda, S. K.; Materia, M. E.; Nigmatullin, R.; Cabrera, D.; Marotta, R.; Cabada, T. F.; Marcello, E.; Nitti, S.; Artes-Ibanez, E. J.; Basnett, P.; Wilhelm, C.; Teran, F. J.; Roy, I.; Pellegrino, T. Esterase-Cleavable 2D Assemblies of Magnetic Iron Oxide Nanocubes: Exploiting Enzymatic Polymer Disassembling To Improve Magnetic Hyperthermia Heat Losses. *Chem. Mater.* **2019**, *31*, 5450−5463.
(24) Chen, R.; Christiansen, M. G.; Sourakov, A.; Mohr, A.; Matsumoto, Y.; Okada, S.; Jasanoff, A.; Anikeeva, P. High-Performance Ferrite Nanoparticles through Nonaqueous Redox Phase Tuning. *Nano Lett.* **2016**, *16*, 1345−1351.
(25) Sharifi Dehsari, H.; Heidari, M.; Halda Ribeiro, A.; Tremel, W.; Jakob, G.; Donadio, D.; Potestio, R.; Asadi, K. Combined Experimental and Theoretical Investigation of Heating Rate on Growth of Iron Oxide Nanoparticles. *Chem. Mater.* **2017**, *29* (22), 9648−9656.
(26) Lak, A.; Niculaes, D.; Anyfantis, G. C.; Bertoni, G.; Barthel, M. J.; Marras, S.; Cassani, M.; Nitti, S.; Athanassiou, A.; Giannini, C.; Pellegrino, T. Facile Transformation of FeO/Fe3O4 Core-Shell Nanocubes to Fe3O4 via Magnetic Stimulation. *Sci. Rep.* **2016**, *6*, 1−12.
(27) Estrader, M.; López-Ortega, A.; Golosovsky, I. V.; Estradé, S.; Roca, A. G.; Salazar-Alvarez, G.; López-Conesa, L.; Tobia, D.; Winkler, E.; Ardisson, J. D.; Macedo, W. A. A.; Morphis, A.; Vasilakaki, M.; Trohidou, K. N.; Gukasov, A.; Mirebeau, I.; Makarova, O. L.; Zysler, R. D.; Peiró, F.; Baró, M. D.; Bergström, L.; Nogués, J. Origin of the Large Dispersion of Magnetic Properties in Nanostructured Oxides: Fe $_x$ O/Fe $_3$O$_4$ Nanoparticles as a Case Study. *Nanoscale* **2015**, *7* (7), 3002−3015.
(28) Evans, B. J.; Hafner, S. S. 57Fe Hyperfine Fields in Magnetite (Fe3O4). *J. Appl. Phys.* **1969**, *40* (3), 1411−1413.
(29) Gorski, C. A.; Scherer, M. M. Determination of Nanoparticulate Magnetite Stoichiometry by Mossbauer Spectroscopy, Acidic Dissolution, and Powder X-Ray Diffraction: A Critical Review. *Am. Mineral.* **2010**, *95* (7), 1017−1026.
(30) Aragón, R.; Buttrey, D. J.; Shepherd, J. P.; Honig, J. M. Influence of Nonstoichiometry on the Verwey Transition. *Phys. Rev. B: Condens. Matter Mater. Phys.* **1985**, *31* (1), 430−436.
(31) Abe, K.; Miyamoto, Y.; Chikazumi, S. Magnetocrystalline Anisotropy of Low Temperature Phase of Magnetite. *J. Phys. Soc. Jpn.* **1976**, *41* (6), 1894−1902.
(32) Marcano, L.; Munoz, D.; Martín-Rodríguez, R.; Orue, I.; Alonso, J.; García-Prieto, A.; Serrano, A.; Valencia, S.; Abrudan, R.; Fernández Barquín, L.; García-Arribas, A.; Muela, A.; Fdez-Gubieda, M. L. Magnetic Study of Co-Doped Magnetosome Chains. *J. Phys. Chem. C* **2018**, *122* (13), 7541−7550.
(33) Bronstein, L. M.; Shtykova, E. V.; Malyutin, A.; Dyke, J. C.; Gunn, E.; Gao, X.; Stein, B.; Konarev, P. V.; Dragnea, B.; Svergun, D. I. Hydrophilization of Magnetic Nanoparticles with Modified Alternating Copolymers. Part 1: The Influence of the Grafting. *J. Phys. Chem. C* **2010**, *114*, 21900−21907.
(34) Peng, E.; Choo, E. S. G.; Tan, C. S. H.; Tang, X.; Sheng, Y.; Xue, J. Multifunctional PEGylated Nanoclusters for Biomedical Applications. *Nanoscale* **2013**, *5* (13), 5994−6005.
(35) Di Corato, R.; Quarta, A.; Piacenza, P.; Ragusa, A.; Figuerola, A.; Buonsanti, R.; Cingolani, R.; Manna, L.; Pellegrino, T. Water Solubilization of Hydrophobic Nanocrystals by Means of Poly(Maleic Anhydride-Alt-1-Octadecene). *J. Mater. Chem.* **2008**, *18* (17), 1991−1996.
(36) Mefford, O. T.; Carroll, M. R. J.; Vadala, M. L.; Goff, J. D.; Mejia-Ariza, R.; Saunders, M.; Woodward, R. C.; St. Pierre, T. G.; Davis, R. M.; Riffle, J. S. Size Analysis of PDMS-Magnetite Nanoparticle Complexes: Experiment and Theory. *Chem. Mater.* **2008**, *20* (6), 2184−2191.
(37) Saville, S. L.; Woodward, R. C.; House, M. J.; Tokarev, A.; Hammers, J.; Qi, B.; Shaw, J.; Saunders, M.; Varsani, R. R.; St Pierre, T. G.; et al. The Effect of Magnetically Induced Linear Aggregates on Proton Transverse Relaxation Rates of Aqueous Suspensions of Polymer Coated Magnetic Nanoparticles. *Nanoscale* **2013**, *5* (5), 2152−2163.
(38) Gandia, D.; Gandarias, L.; Rodrigo, I.; Robles-Garcia, J.; Das, R.; Garaio, E.; Garcia, J. A.; Phan, M.-H.; Srikanth, H.; Orue, I.; Alonso, J.; Muela, A.; Fdez-Gubieda, M. L. Unlocking the Potential of Magnetotactic Bacteria as Magnetic Hyperthermia Agents. *Small* **2019**, *15*, 1970222.
(39) Carrey, J.; Mehdaoui, B.; Respaud, M. Simple Models for Dynamic Hysteresis Loop Calculations of Magnetic Single-Domain Nanoparticles: Application to Magnetic Hyperthermia Optimization. *J. Appl. Phys.* **2011**, *109* (8), 083921.
(40) Rodrigo, I.; Castellanos-Rubio, I.; Garaio, E.; K. Arriortua, O.; Insausti, M.; Orue, I.; García, J. Á.; Plazaola, F. Accurate Measurements of the Dynamic Hysteresis Loops and Heating Mechanisms via High Field, High Frequency and Temperature Adjustable AC Magnetometer for Magnetic Hyperthermia Characterization. *Int. J. Hyperth.* **2020** Submitted for publication.
(41) Le, P. U.; Guay, G.; Altschuler, Y.; Nabi, I. R. Caveolin-1 Is a Negative Regulator of Caveolae-Mediated Endocytosis to the Endoplasmic Reticulum. *J. Biol. Chem.* **2002**, *277* (5), 3371−3379.
(42) Rejman, J.; Oberle, V.; Zuhorn, I. S.; Hoekstra, D. Size-Dependent Internalization of Particles via the Pathways of Clathrin- and Caveolae-Mediated Endocytosis. *Biochem. J.* **2004**, *377*, 159−169.
(43) Muro, S.; Koval, M.; Muzykantov, V. Endothelial Endocytic Pathways: Gates for Vascular Drug Delivery. *Curr. Vasc. Pharmacol.* **2004**, *2* (3), 281−299.
(44) Wang, D.; Tong, Y.; Li, Y.; Tian, Z.; Cao, R.; Yang, B. Diamond & Related Materials PEGylated Nanodiamond for Chemotherapeutic Drug Delivery. *Diamond Relat. Mater.* **2013**, *36*, 26−34.
(45) Feng, Q.; Liu, Y.; Huang, J.; Chen, K.; Huang, J.; Xiao, K. Uptake, Distribution, Clearance, and Toxicity of Iron Oxide Nanoparticles with Different Sizes and Coatings. *Sci. Rep.* **2018**, *8*, 1−13.
(46) Guarnieri, D.; Guaccio, A.; Fusco, S.; Netti, P. A. Effect of Serum Proteins on Polystyrene Nanoparticle Uptake and Intracellular Trafficking in Endothelial Cells. *J. Nanopart. Res.* **2011**, *13*, 4295−4309.
(47) Chithrani, B. D.; Ghazani, A. A.; Chan, W. C. W. Determining the Size and Shape Dependence of Gold Nanoparticle Uptake into Mammalian Cells. *Nano Lett.* **2006**, *6* (4), 662−668.
(48) Castellanos-Rubio, I.; Munshi, R.; Qadri, S.; Pralle, A. Nanoparticle Preparation for Magnetothermal Genetic Stimulation

https://dx.doi.org/10.1021/acsami.0c03222
ACS Appl. Mater. Interfaces 2020, 12, 27917−27929

in Cell Culture and in the Brain of Live Rodents. *Neuromethods* **2018**, *135*, 39−51.
(49) Garaio, E.; Collantes, J. M.; Plazaola, F.; Garcia, J. A.; Castellanos-Rubio, I. A Multifrequency Eletromagnetic Applicator with an Integrated AC Magnetometer for Magnetic Hyperthermia Experiments. *Meas. Sci. Technol.* **2014**, *25* (11), 115702.

https://dx.doi.org/10.1021/acsami.0c03222
ACS Appl. Mater. Interfaces 2020, 12, 27917−27929